Research Article | Vol. 31, No. 15 / 17 Jul 2023 / Optics Express 24862
Optics EXPRESS

In-line synthesis of multi-octave phase-stable infrared light

HADIL KASSAB,[1] SEBASTIAN GRÖBMEYER,[1,2] WOLFGANG SCHWEINBERGER,[2,3] CHRISTINA HOFER,[1,3,4,5] PHILIPP STEINLEITNER,[1,2] MAXIMILIAN HÖGNER,[1,2] TATIANA AMOTCHKINA,[1] DANIEL GERZ,[2,6] MATTHIAS KNORR,[7] RUPERT HUBER,[7] NICHOLAS KARPOWICZ,[1,2] AND IOACHIM PUPEZA[1,2,6,*]

[1]*Max Planck Institute of Quantum Optics, Hans-Kopfermann-Str. 1, 85748 Garching, Germany*
[2]*Ludwig Maximilian University Munich, Am Coulombwall 1, 85748 Garching, Germany*
[3]*Center for Molecular Fingerprinting, Nonprofit LLC, 1093 Budapest, Czuczor utca 2-10, Hungary*
[4]*Department of Physics and Astronomy, University of British Columbia, Vancouver, British Columbia V6T 1Z1, Canada*
[5]*Quantum Matter Institute, University of British Columbia, Vancouver, BC, V6T 1Z4, Canada*
[6]*Leibniz Institute of Photonic Technology - Member of the Research Alliance "Leibniz Health Technologies", Albert-Einstein-Straße 9, Jena, Germany*
[7]*Department of Physics, University of Regensburg, 93040 Regensburg, Germany*
[*]*ioachim.pupeza@mpq.mpg.de*

Abstract: Parametric downconversion driven by modern, high-power sources of 10-fs-scale near-infrared pulses, in particular intrapulse difference-frequency generation (IPDFG), affords combinations of properties desirable for molecular vibrational spectroscopy in the mid-infrared range: broad spectral coverage, high brilliance, and spatial and temporal coherence. Yet, unifying these in a robust and compact radiation source has remained a key challenge. Here, we address this need by employing IPDFG in a multi-crystal in-line geometry, driven by the 100-W-level, 10.6-fs pulses of a 10.6-MHz-repetition-rate, nonlinearly post-compressed Yb:YAG thin-disk oscillator. Polarization tailoring of the driving pulses using a bichromatic waveplate is followed by a sequence of two crystals, $LiIO_3$ and $LiGaS_2$, resulting in the simultaneous coverage of the 800-cm^{-1}-to-3000-cm^{-1} spectral range (at -30-dB intensity) with 130 mW of average power. We demonstrate that optical-phase coherence is maintained in this in-line geometry, in theory and experiment, the latter employing ultra-broadband electro-optic sampling. These results pave the way toward coherent spectroscopy schemes like field-resolved and frequency-comb spectroscopy, as well as nonlinear, ultrafast spectroscopy and optical-waveform synthesis across the entire infrared molecular fingerprint region.

1. Introduction

Asymmetric charge distributions in molecules are responsible for the efficient coupling of infrared (IR) radiation to fundamental ro-vibrational modes of the constituent (groups of) atoms via electric dipole moments [1]. The eigenfrequencies, strengths, and decay times of these molecular-scale oscillations are determined by the atomic constituents, their conformation, and dynamics. This results in a spectroscopic "fingerprint" unique to the molecular sample, and experimentally accessible via probing with broadband IR light. Consequently, IR spectroscopy serves a broad gamut of applications [2]ranging from fundamental science [1,3] over chemical analysis [4] to biology and medicine [5].

Two highly desirable properties of IR sources for molecular fingerprinting are (i) broad bandwidth, ideally covering the entire molecular fingerprint region (usually defined to start at 2.8

#493887 https://doi.org/10.1364/OE.493887
Journal © 2023 Received 27 Apr 2023; revised 9 Jun 2023; accepted 11 Jun 2023; published 12 Jul 2023

Optics EXPRESS

μm – or 3700 cm^{-1} – corresponding to the eigenfrequency of the O-H stretching vibration), and (ii) high brilliance, translating to sample-specific IR fingerprints strong enough to be detectable [6]. In addition, (iii) spatial coherence and (iv) temporal coherence enable advanced spectroscopy schemes. Most prominently, spatial coherence allows for long interaction lengths / multiple passes through gaseous samples enhancing the sensitivity, and the frequency-comb nature of phase-controlled broadband light enables high-resolution spectroscopy with accurate absolute-frequency calibration [7–14]. Equally importantly, temporal coherence affords an outstanding control over (and reproducibility of) broadband optical waveforms. In time-domain spectroscopy techniques, the confinement of broadband optical spectra to merely a few, highly controlled oscillations of the optical wave can be used, for instance, to probe the nonlinear response of matter to an intensive excitation on the level of the electric field of light [15,16]. The temporal confinement of a broadband excitation has been shown to possess sensitivity advantages even in linear spectroscopy, stemming from the temporal separation of the sample-specific response from the – often orders-of-magnitude – stronger and shorter excitation [17].

In recent years, coherent IR sources based on femtosecond lasers have demonstrated the feasibility of different combinations of the properties (i)-(iv), see, e.g., [10,17–35] and references therein. Yet, simultaneously achieving these properties in a robust and compact source has remained a challenge. Here, we address this challenge employing intra-pulse difference-frequency generation (IPDFG) in a multi-crystal in-line geometry, driven by the high-power 10-fs-scale pulses of a 10.6-MHz-repetition-rate, nonlinearly post-compressed Yb:YAG thin-disk oscillator.

2. Yb-based femtosecond frontend

The initial pulse train in our setup is produced by a Kerr-lens mode-locked Yb:YAG thin-disk oscillator with a repetition frequency of 10.6 MHz, previously described in Ref. [36]. At an average output power of 140 W, this frontend operates in air and delivers pulses with a duration of 300 fs, spectrally centred at 1030 nm. To achieve the 10-fs-scale pulse durations necessary for broadband IPDFG, with high throughput efficiency, we employed extra-cavity pulse compression based on multiple passes through thin Kerr media [37–41]. Specifically, 120 W from the oscillator output were sent to a dual-stage Herriott-cell-type spectral broadening along with subsequent chirped mirrors [42], followed by a distributed quasi-waveguide [43]. The pulse durations after the first two compression stages were 68 fs and 16 fs, respectively. The last stage consisted of four individual plates and chirped mirrors for temporal re-compression after the third one and was designed to provide fine control over nonlinearity and dispersion. At the output, 10.6-fs linearly-polarized pulses with a Fourier-transform-limited duration of 9.8 fs, an average power of 100 W, and an M^2 value of 1.2 were measured.

3. Polarization-tailored multi-crystal IPDFG

When driven with 10-fs-scale near-IR pulses, the 2nd-order parametric process of IPDFG [32,44,45] (also known as "optical rectification") can, in principle, result in the coverage of the entire IR molecular fingerprint region. In addition, if higher-order (cascaded) nonlinearities are negligible, the waveforms obtained by IPDFG exhibit outstanding passive optical-phase stability [46], because the nonlinear polarization responsible for the emitted IR electric field follows the cycle-averaged intensity envelope of the driving pulse [47]. Its conceptual simplicity, together with the excellent temporal coherence, make IPDFG-based IR sources highly promising candidates for unifying the properties (i)-(iv) listed in the Introduction, in particular in the context of modern, high-power, compact near-IR femtosecond lasers [10,11,14,17–21,24–26,31]. In the following, we demonstrate how using the train of nonlinearly-compressed pulses described in the previous section in an in-line multi-crystal arrangement fulfills this promise.

In our setup, 4% of the power of the temporally-compressed near-IR pulses was split off for field-resolved detection (discussed in the next section) via reflection off a wedge (Fig. 1(a)).

Optics EXPRESS

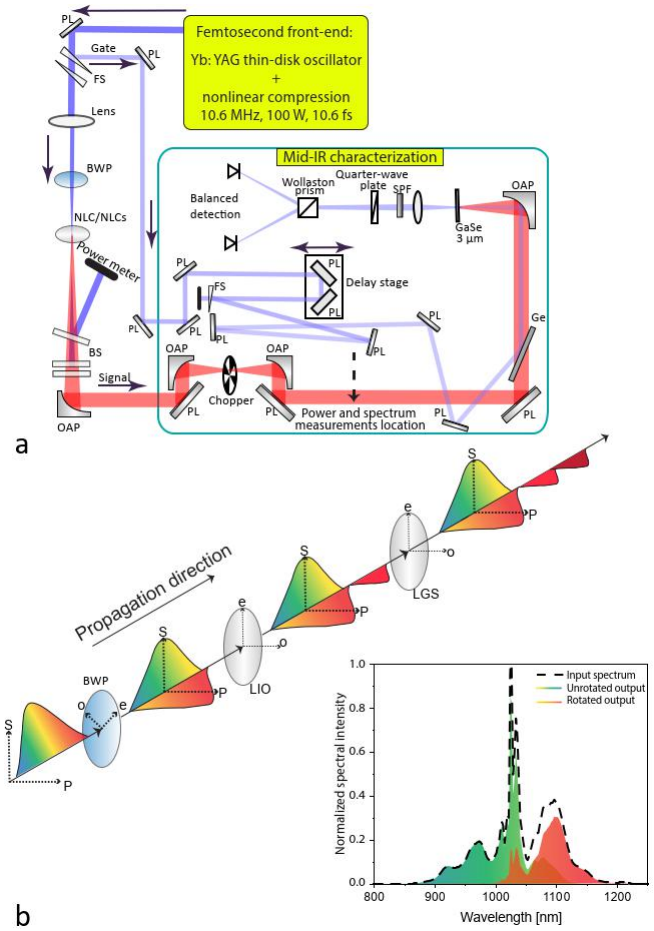

Fig. 1. (a) Schematic of the experimental setup, see text. PL: plane mirror, OAP: off-axis parabola, FS: fused silica wedge, NLC/NLCs: nonlinear crystal(s), BWP: bichromatic waveplate, Ge: germanium, SPF: short-pass filter. A 3 mm Ge plate was used as a beam combiner for the mid-IR and the near-IR gate beam. At the angle of incidence of 80° for the incident p-polarized mid-IR beam and for the s-polarized near-IR beam. The Ge plate transmitted and reflected the majority of the mid-IR and gate beams, respectively. (b) Polarization distribution and evolution of the spectra upon propagation through the crystals, with respect to the ordinary (o) and extraordinary (e) optical axes of the crystals. The colors represent the spectral distributions on the axes (and not temporal information). The inset shows the intensity spectra (colored) measured after the BWP on the two polarization axes, normalized to the maximum of the input spectrum (dashed line).

Optics EXPRESS

A second wedge removed spatial chirp and, together with a chirped mirror, was used to compensate for the chromatic dispersion of subsequent optical elements. A 500-mm focal-length lens was used to generate a focus with a 40-µm $1/e^2$-intensity radius.

IPDFG was driven in two different crystals, $LiIO_3$ (LIO) and $LiGaS_2$ (LGS). To maximize the conversion efficiency while simultaneously reaching a broad spectral coverage, type-I phase matching was used for both crystals. Rotating the polarization of the lower-frequency part of the driving spectrum (signal) with respect to the high-frequency part (pump) utilizing a bichromatic waveplate (BWP), see Fig. 1(b), provides a convenient way to optimize the polarization distribution of the driving field for type-I phase matching [25,32–34,48]. Here, we have employed a BWP consisting of a combination of three quartz plates mounted with air gaps, each plate having antireflection coatings on both sides (manufactured by B. Halle). The three quartz plates have the thicknesses 3.4, 2.2 and 1.4 mm and are mounted at 0°, -53° and 0° with respect to the slow axis, respectively. The orientations of the effective fast and slow axes of the combination vary over the spectrum. In the 1150-to-1250-nm range, the optic acts as a nearly achromatic half-wave plate with a polarization rotation by 90°, whereas in the 880-to-980-nm range the BWP leaves the polarization unchanged. The inset in Fig. 1(b) shows the near-IR spectra measured in the two polarizations after the BWP.

Following the BWP, a 400-µm-thick LIO crystal was used to cover the high-frequency mid-IR range, with wavenumbers above ~1850 cm^{-1}, where LIO becomes opaque being an oxide. The protection-coated crystal was oriented with its e-axis along the polarization direction of the higher-frequency components of the near-IR light after the BWP, and was tilted to extend the high-frequency cut-off as far as possible. The angles for type-I (e-o-o) phase-matched IPDFG were $\varphi = 0°$ and $\theta = 20°$. By systematically shifting several LIO crystals toward the focus, the damage threshold was experimentally determined to be at a peak intensity of around 76 GW/cm^2, reached at a near-IR beam radius of 0.8 mm. For the IPDFG experiments, the crystal was placed behind the focus, with an estimated peak intensity 10% lower than the damage threshold.

In order to separate the generated IR light from the driving pulses, an ultra-broadband beam splitter was designed and manufactured in-house (Fig. 1(a), BS) [49]. The beam splitter deposited on a 1-mm thick ZnSe substrate consists of ZnS and YbF3 layers. The back side of the substrate was coated by a ZnS/YbF3 anti-reflection coating. Its front side, while transmitting in the mid-IR range (see transmission curve shown in Fig. 2(a)), is highly reflective (spectral average of 90%) for the near-IR spectrum. To suppress the unconverted near-IR power, we used a sequence of three such optics, followed by an additional 3-mm Ge plate, anti-reflection-coated in the range between 3 µm and 12 µm.

By accounting for the transmission and reflection properties of all optics used between the LIO crystal and the position of the IR power measurement (see Fig. 1(a)), we estimated an average output power directly after the crystal of 30 mW. The generated spectrum, measured with a Fourier-transform infrared (FTIR) spectrometer (see setup in Fig. 1(a)) is shown in Fig. 2(a) (magenta, continuous line).

In analogy to IPDFG driven in LIO, in a second experiment, IPDFG was driven in an uncoated 300-µm LGS crystal, cut in the x-z plane, and set up for type-I phase matching with $\varphi = 0°$ and $\theta = 48°$. The crystal was placed at a near-IR beam radius of 0.87 mm, corresponding to a peak intensity of 56 GW/cm^2 and was tilted to favor phase matching for lower mid-IR frequencies. The output power behind the LGS crystal was 102 mW. The power spectral density is shown in Fig. 2(a) (blue, continuous line).

The influence of the first crystal on the IPDFG in the second one in terms of driving pulse dispersion or depolarization was minor/negligible, as confirmed by the MIR power generated in the two-crystal case approaching the sum of powers for IPDFG in the individual crystals, as well as by the linear polarization of the generated MIR radiation. Placing both crystals collinearly (first LIO, second LGS) resulted in continuous spectral coverage of more than 2

Optics EXPRESS

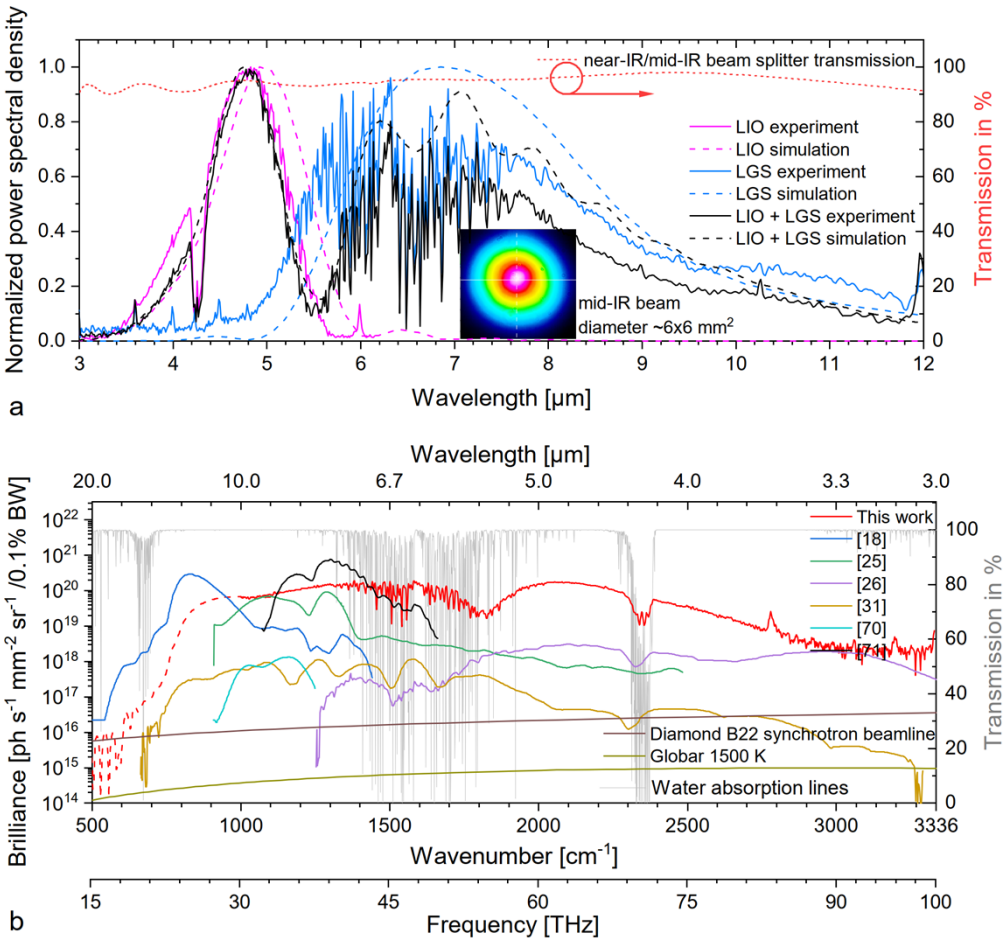

Fig. 2. (a) Transmission of the near-IR/mid-IR beam splitter (red, dashed line, right y-axis), and experimental spectra (continuous lines, measured with an FTIR spectrometer and normalized to their respective maxima), for LIO and LGS individually, as well as for their in-line sequence. Dashed lines: results of numerical simulations for all configurations. (b) Brilliance comparison of our source (red) with a representative selection of 1-µm-driven IPDFG-based coherent mid-IR sources. Grey lines (and right y-axis): transmission through 1 m of laboratory air [68], approximating the mid-IR beam path in our setup from generation to detection. The brilliance curve for our experiment is stitched from two measurements: via FTIR spectrometer (continuous, red line) above 1000 cm^{-1} (limited by the detector at smaller wavenumbers) and via EOS (dashed, red line) below 1000 cm^{-1}. EOS provides a broader detectivity range toward smaller wavenumbers (see instrument response function in Fig. 3). The EOS curve was stitched to the FTIR curve in the 500-to-1000-cm^{-1} range, where the spectral shapes match.

Optics EXPRESS

octaves (Fig. 2(a), black, continuous line). The total average power after the second crystal with the BWP in place was determined to be approximately 130 mW, as compared to 35 mW without the BWP. A slight mismatch between the sum of the powers in single-crystal configuration and the total power in tandem configuration is attributed to alignment differences and propagation effects through the first crystal. The LIO crystal was anti-reflection coated for the NIR spectral range, minimizing losses upon Fresnel reflection. The broadband IR beam was collimated by an unprotected gold-coated off-axis parabola (OAP) to a diameter of ~6 mm, with the intensity profile of the beam shown in the inset in Fig. 2(a). Figure 2(b) compares the brilliance of our IR source to the state of the art of 1-μm-driven IPDFG sources, as well as to that of a 3rd-generation IR synchrotron beamline and that of widely-employed thermal sources [50].

4. Phase stability of the synthesized optical field

Besides the simplicity and compactness of IPDFG, one highly attractive feature is its passive optical-phase stability [32]. However, for a free-running femtosecond frontend – that is, without stabilization of the optical phase of the pulse train that drives IPDFG – the resulting mid-IR radiation only exhibits passive phase stability if there is no process mixing the optical phase of the driving pulses into the mid-IR field. This condition is, for instance, not fulfilled when cascading nonlinear processes are involved [24,51]. In our case, the combination of the central wavelength of the driving pulses, phase matching and relatively low nonlinearity avoids cascading nonlinearities and allows for the coverage of the entire molecular fingerprint region with waveform-stable light. At the same time, the central wavelength of 1030 nm of the driving pulses (with uncontrolled optical phase) enables their spectral separation from the targeted mid-IR molecular fingerprint region. In the following, we discuss the numerical as well as experimental verification of the optical-phase stability of the polarization-tailored multi-crystal IPDFG source.

To build a theoretical understanding of the nonlinear processes occurring in the crystals, we modeled these effects numerically employing the nonlinear wave equation in the slowly-evolving wave approximation [52]. We use literature values for the refractive indices and nonlinear coefficients of LGS [53], LIO [54], and GaSe [55,56], accounting for 2nd and 3rd order nonlinearities. The system was solved on a uniform, three-dimensional grid (two spatial dimensions, plus time) and propagated numerically in space through the optical system.

In the full simulation, the electric field, whose temporal intensity was determined by a frequency-resolved optical gating measurement, and assumed to be Gaussian in space, propagated nonlinearly through the LIO crystal, propagated through 11 mm of free space, then propagated nonlinearly through the LGS crystal. Finally, the carrier-envelope phase (CEP) and pulse energy of the input pulse were scanned in order to determine their influence on the noise characteristics of the final IPDFG field. The results for the mid-IR power spectral densities obtained with the numerical simulations are shown with dashed lines in Fig. 2(a) for the three configurations (LIO, LGS, LIO followed by LGS). The agreement with the measured spectra validates our numerical model.

In order to numerically verify the optical-phase stability of the generated mid-IR radiation, we repeated simulations with the CEP phase of the near-IR driving pulses varied from 0 to 2π in steps of $\pi/8$ rad and otherwise identical input values. The temporal phase of the resulting mid-IR field varied by less than 1 μrad in the output bandwidth, which is expected to be negligible in applications.

To confirm the theoretically predicted mid-IR waveform stability, we implemented an electro-optic sampling (EOS) setup [57–60]. As the gate pulse, we used a copy of the near-IR driving pulse, reflectively attenuated to an average power of 80 mW at the EOS crystal. After the spatial combination of the mid-IR wave with the near-IR gate pulse train at an uncoated Ge plate (Fig. 1(a)), the collinear beams were focused onto the EOS crystal by an unprotected gold-coated

Optics EXPRESS

90° off-axis parabola. At the focus, the radius values were $43 \times 60\ \mu m^2$ and $58 \times 58\ \mu m^2$ for the gate and the mid-IR beams, respectively.

Capturing the entire bandwidth of the generated mid-IR field at once requires an ultrabroadband electro-optic sensor. To this end, as well as to record a signal that closely resembles the actual optical electric field, we opted for a 3-µm-thin GaSe crystal optically contacted on a 0.5-mm CVD (chemical vapor deposition) diamond plate [61]. This assembly combines the advantages of an ultra-broadband instrument response with the suppression of multiple reflections (echo effect) inside the EOS crystal. Following the GaSe-crystal-on-diamond assembly, the EOS detection consisted of a Wollaston prism, a 950-nm short-pass filter, and an electronically-balanced detector with two Si photodiodes. Lock-in detection was used, mechanically chopping the mid-IR beam at 6 kHz. The instrument response function calculated with our numerical model, including the nonlinear propagation in the GaSe crystal and filtered detection of the resulting polarization state of the gate pulse, is plotted in Fig. 3. It exhibits a broadband, flat spectral response up to 2000 cm^{-1}, with a suppression of higher wavenumbers.

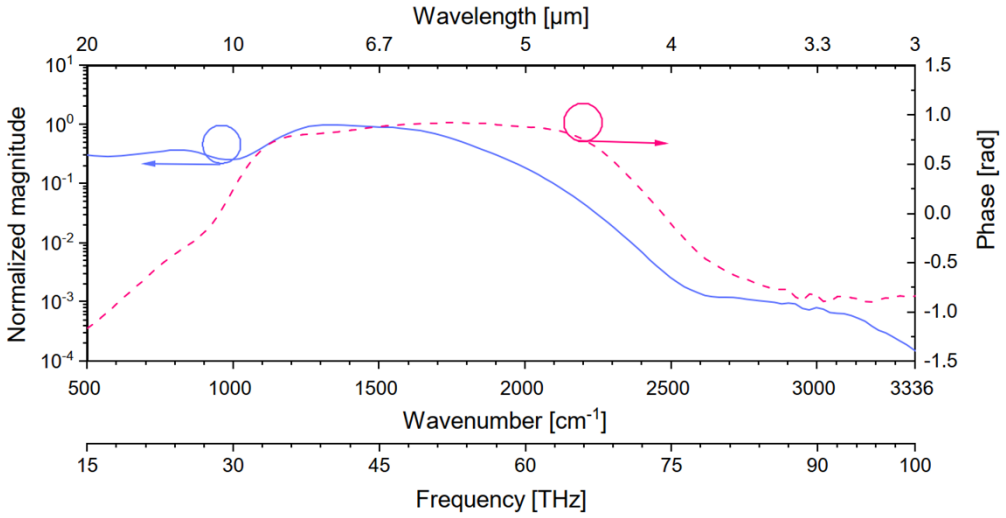

Fig. 3. Spectral magnitude (normalized to its maximum, blue, continuous line) and spectral phase (red, dashed line) of the EOS instrument response function (see text). Note that the response in the absorption of GaSe near 500 cm^{-1} is likely to be distorted by features of the complex refractive index not included in the Sellmeier equation used [55,56,69].

Figure 4 shows EOS measurements of the three configurations: LIO only (Fig. 4(a)), LGS only (Fig. 4(b)), and LIO followed by LGS (Fig. 4(c)). The individual traces are baseline-corrected, power-normalized, and delay-shifted to compensate for minor power and delay drifts of the laser system and of the detection interferometer. In detail, slight drifts in the balanced detection are compensated via a constant shift of the baseline while drifts in power and delay are corrected by minimizing the deviations between the individual full scans by scaling the amplitude and shifting the position of each scan separately. The insets present simulation results performed with near-IR driving pulses having opposing CEP values, and illustrating the expected optical-phase stability of the generated mid-IR field. The statistics of the measured EOS traces exhibit similar values for all cases, confirming the mid-IR waveform stability within our measurement uncertainty. Fluctuations appear the weakest in the first zoom-in, to the above-mentioned pre-processing steps. In addition to the normalization, the relative effect of detection noise, as well as laser and interferometer drifts increase towards longer delays. Inter-trace timing jitter, which can be

Optics EXPRESS

attributed to a long interferometer, is strongest visible in the middle panels, showing the zero crossings of the waveform.

Optics EXPRESS

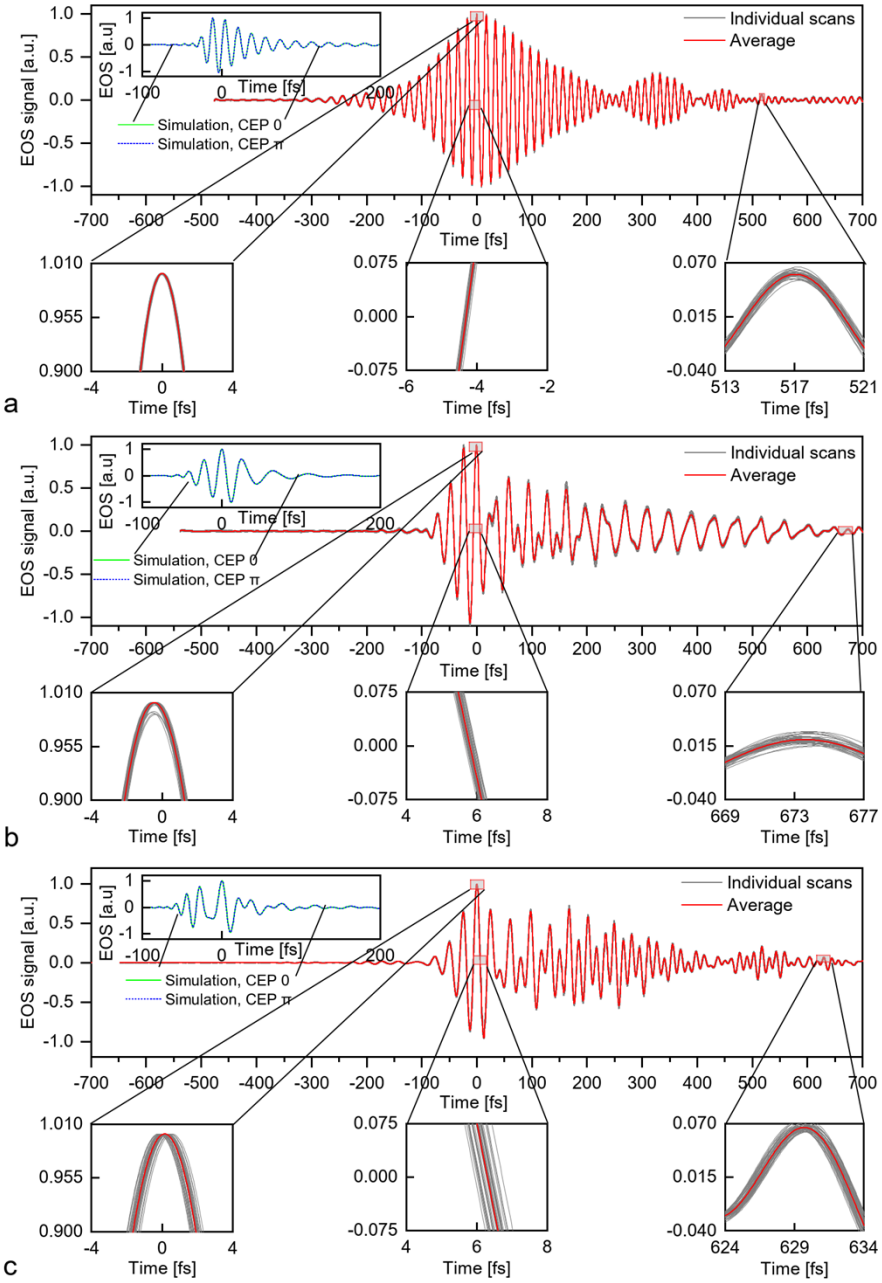

Fig. 4. Waveform stability. EOS measurements for (a) LIO only, (b) LGS only, and (c) LIO followed by LGS. The measurements shown in panel c have been taken on a different day than those in panels a and b, with a slightly worse noise performance of the laser system. For each configuration, 40 individual scans are shown (grey), with a measurement time of 4.5 seconds per scan. Red lines: average of recorded scans. Insets: simulated EOS traces for near-IR driving pulses having opposing CEP values, illustrating the independence of the waveform obtained via IPDFG thereof. The deviation of the measured waveform from a Fourier-transform-limited pulse is caused by strong absorptions in the molecules making up the laboratory atmosphere, by propagation through the 3-mm of ZnSe substrate of the NIR/MIR beam splitters, the 2-mm Ge beam combiner for EOS, and the EOS response function. Careful management of these contributions, along with MIR dispersive mirrors hold the potential of temporally compressing the measured waveforms.

Optics EXPRESS

5. Conclusions and outlook

In conclusion, we have presented a femtosecond-laser-based IR radiation source combining – for the first time to the best of our knowledge – all the properties desirable for broadband spectroscopy in the molecular fingerprint region: broad spectral coverage with a brilliance exceeding that of synchrotron IR beamlines by more than 2 orders of magnitude over the entire molecular fingerprint region (and up to 4 orders of magnitude), and spatial as well as temporal coherence. At the same time, our femtosecond source preserves the conceptual simplicity of an in-line setup. The simultaneous coverage of the entire molecular fingerprint region was achieved by IPDFG driven in two consecutive crystals, thus combining their phase-matching bandwidths. Tailoring the polarization distribution for the input field resulted in record brilliance values for 1-µm-driven IPDFG sources. Table 1 summarizes the most important experimental parameters, in the context of state-of-the-art 1-µm-driven IPDFG sources.

Table 1. Parameters of state-of-the-art 1-µm-driven IPDFG sources.[a]

NIR peak intensity [GW/ cm^2]	Nonlinear crystal	IPDFG spectral span [µm] (at -30 dB intensity)	Mid-IR power [mW]	Power conversion efficiency [%]	Reference
76, 54	LIO and LGS	3.4-15	130	0.147	This work
350	LGS	6.7-18	103	0.2	[18]
150	LGS	5-11	31.8	0.16	[25]
130	LGS	8-11	0.37	0.04	[70]
250	LIO	2.5-8	1.1	0.003	[26]
90	ZnS	3-15	0.8	0.02	[31]
140, 300	LGS and LGS	6-9	160	2	[71]

[a]The peak intensity values are given as stated in the papers if available, and otherwise calculated as $I = P_p/A$, where $P_p = E_p/T$ and $A = \pi(r/2)^2$ denote the pulse peak power and area of a Gaussian beam, respectively. T and r denote the pulse duration and the beam radius, respectively.

We have verified the coherence properties of the source both in theory and experiment, the latter employing ultra-broadband electro-optic sampling. In our arrangement, the spectral content and chirp of the NIR driving pulse train have two effects on the generated MIR waveforms. Firstly, the latter are generated with identically repeating electric fields, in particular in the range where the spectra individually generated in the two crystals, overlap. While a full study of the conditions under which this holds lies beyond the scope of this paper, we note that our results demonstrate the feasibility of coherent spectral synthesis. Secondly, they affect the shape of these reproducible waveforms (which is approximatively reproduced by the broadband EOS detection). This is likely to provide a means for tailoring specific waveforms. In accordance with the stability of the NIR femtosecond frontend in terms of spectral content and chirp over the time scale of several hours, both aforementioned properties were conserved in our experiment on the same time scale.

Besides being readily suitable for Fourier-transform spectroscopy, this source enables advanced spectroscopy schemes drawing from its temporal coherence. In particular, the offset-free (that is, single-parameter) frequency-comb nature of the spectrum of the high-repetition-rate phase-stable waveforms promises convenient implementations of ultra-broadband mid-IR frequency-comb [62], dual-comb [11,12,63] and cavity-enhanced [64] spectroscopy over the entire molecular fingerprint region, just to name a few examples. In addition, the waveform stability enables high-sensitivity field-level detection [6,11,16–20,24,25,27,30,51,61].

The generated mid-IR pulses with an energy of 12.3 nJ support a Fourier-transform limit of 13 fs. When tightly focused, field strengths well into the multi-MV/cm come into reach, extending

Optics EXPRESS

the scope of this source to (field-resolved) nonlinear spectroscopy schemes [15,65]. The fact that the multi-crystal IPDFG arrangement preserves phase stability promises the feasibility of generalizing this scheme toward synthesis of waveforms [66,67] with specific shapes. In addition, covering even broader bandwidths, in particular toward lower IR frequencies with waveform-stable light seems feasible.

Funding. Max-Planck-Institut für Quantenoptik; Max Planck Technology Transfer program; Max Planck School of Photonics; Centre for Advanced Laser Applications; Max-Planck-Gesellschaft; Deutsche Forschungsgemeinschaft under Germany's Excellence Strategy (EXC 2051, Project-ID 390713860, (project A05), Research grat HU1598/8); Canada First Research Excellence Fund; Quantum Materials and Future Technologies Program; Natural Sciences and Engineering Research Council of Canada.

Acknowledgments. The authors acknowledge fruitful discussions with Ferenc Krausz and Kafai Mak.

Disclosures. The authors declare no conflicts of interest.

Data availability. Data underlying the results presented in this paper are not publicly available at this time but can be obtained from the authors upon reasonable request.

References

1. W. Demtröder, *Molecular Physics: Theoretical Principles and Experimental Methods* (John Wiley & Sons, 2008).
2. S. S. Dhillon, M. S. Vitiello, and E. H. Linfield, *et al.*, "The 2017 terahertz science and technology roadmap," J. Phys. D: Appl. Phys. **50**(4), 043001 (2017).
3. R. Mankowsky, M. Först, and A. Cavalleri, "Non-equilibrium control of complex solids by nonlinear phononics," Rep. Prog. Phys. **79**(6), 064503 (2016).
4. J. Haas and B. Mizaikoff, "Advances in Mid-Infrared Spectroscopy for Chemical Analysis," Annu. Rev. Anal. Chem. **9**(1), 45–68 (2016).
5. M. J. Baker, J. Trevisan, and P. Bassan, *et al.*, "Using Fourier transform IR spectroscopy to analyze biological materials," Nat. Protoc. **9**(8), 1771–1791 (2014).
6. M. T. Peschel, M. Högner, T. Buberl, D. Keefer, R. de Vivie-Riedle, and I. Pupeza, "Sub-optical-cycle light-matter energy transfer in molecular vibrational spectroscopy," Nat. Commun. **13**(1), 5897 (2022).
7. T. Udem, R. Holzwarth, and T. W. Hänsch, "Optical frequency metrology," Nature **416**(6877), 233–237 (2002).
8. N. Picqué and T. W. Hänsch, "Frequency comb spectroscopy," Nat. Photonics **13**(3), 146–157 (2019).
9. A. Schliesser, N. Picqué, and T. W. Hänsch, "Mid-infrared frequency combs," Nat. Photonics **6**(7), 440–449 (2012).
10. S. Vasilyev, I. S. Moskalev, V. O. Smolski, J. M. Peppers, M. Mirov, A. V. Muraviev, K. Zawilski, P. G. Schunemann, S. B. Mirov, K. L. Vodopyanov, and V. P. Gapontsev, "Super-octave longwave mid-infrared coherent transients produced by optical rectification of few-cycle 25-μm pulses," Optica **6**(1), 111 (2019).
11. A. S. Kowligy, H. Timmers, A. J. Lind, U. Elu, F. C. Cruz, P. G. Schunemann, J. Biegert, and S. A. Diddams, "Infrared electric field sampled frequency comb spectroscopy," Sci. Adv. **5**(6), eaaw8794 (2019).
12. H. Timmers, A. Kowligy, A. Lind, F. C. Cruz, N. Nader, M. Silfies, G. Ycas, T. K. Allison, P. G. Schunemann, S. B. Papp, and S. A. Diddams, "Molecular fingerprinting with bright, broadband infrared frequency combs," Optica **5**(6), 727 (2018).
13. D. M. B. Lesko, H. Timmers, S. Xing, A. Kowligy, A. J. Lind, and S. A. Diddams, "A six-octave optical frequency comb from a scalable few-cycle erbium fibre laser," Nat. Photonics **15**(4), 281–286 (2021).
14. A. Catanese, J. Rutledge, M. C. Silfies, X. Li, H. Timmers, A. S. Kowligy, A. Lind, S. A. Diddams, and T. K. Allison, "Mid-infrared frequency comb with 6.7 W average power based on difference frequency generation," Opt. Lett. **45**(5), 1248–1251 (2020).
15. O. Schubert, M. Hohenleutner, F. Langer, B. Urbanek, C. Lange, U. Huttner, D. Golde, T. Meier, M. Kira, S. W. Koch, and R. Huber, "Sub-cycle control of terahertz high-harmonic generation by dynamical Bloch oscillations," Nat. Photonics **8**(2), 119–123 (2014).
16. B. Mayer, C. Schmidt, J. Bühler, D. V. Seletskiy, D. Brida, A. Pashkin, and A. Leitenstorfer, "Sub-cycle slicing of phase-locked and intense mid-infrared transients," New J. Phys. **16**(6), 063033 (2014).
17. I. Pupeza, M. Huber, and M. Trubetskov, *et al.*, "Field-resolved infrared spectroscopy of biological systems," Nature **577**(7788), 52–59 (2020).
18. I. Pupeza, D. Sánchez, J. Zhang, N. Lilienfein, M. Seidel, N. Karpowicz, T. Paasch-Colberg, I. Znakovskaya, M. Pescher, W. Schweinberger, V. Pervak, E. Fill, O. Pronin, Z. Wei, F. Krausz, A. Apolonski, and J. Biegert, "High-power sub-two-cycle mid-infrared pulses at 100 MHz repetition rate," Nat. Photonics **9**(11), 721–724 (2015).
19. T. P. Butler, D. Gerz, C. Hofer, J. Xu, C. Gaida, T. Heuermann, M. Gebhardt, L. Vamos, W. Schweinberger, J. A. Gessner, T. Siefke, M. Heusinger, U. Zeitner, A. Apolonski, N. Karpowicz, J. Limpert, F. Krausz, and I. Pupeza, "Watt-scale 50-MHz source of single-cycle waveform-stable pulses in the molecular fingerprint region," Opt. Lett. **44**(7), 1730 (2019).
20. C. Gaida, M. Gebhardt, T. Heuermann, F. Stutzki, C. Jauregui, J. Antonio-Lopez, A. Schülzgen, R. Amezcua-Correa, A. Tünnermann, I. Pupeza, and J. Limpert, "Watt-scale super-octave mid-infrared intrapulse difference frequency generation," Light: Sci. Appl. **7**(1), 94 (2018).

Optics EXPRESS

21. U. Elu, L. Maidment, L. Vamos, F. Tani, D. Novoa, M. H. Frosz, V. Badikov, D. Badikov, V. Petrov, P. St. J. Russell, and J. Biegert, "Seven-octave high-brightness and carrier-envelope-phase-stable light source," Nat. Photonics **15**(4), 277–280 (2021).
22. P. Täschler, M. Bertrand, B. Schneider, M. Singleton, P. Jouy, F. Kapsalidis, M. Beck, and J. Faist, "Femtosecond pulses from a mid-infrared quantum cascade laser," Nat. Photonics **15**(12), 919–924 (2021).
23. Q. Ru, T. Kawamori, P. G. Schunemann, S. Vasilyev, S. B. Mirov, and K. L. Vodopyanov, "Two-octave-wide (3–12 μm) subharmonic produced in a minimally dispersive optical parametric oscillator cavity," Opt. Lett. **46**(4), 709 (2021).
24. P. Steinleitner, N. Nagl, M. Kowalczyk, J. Zhang, V. Pervak, C. Hofer, A. Hudzikowski, J. Sotor, A. Weigel, F. Krausz, and K. Mak, "Single-cycle infrared wavform control," Nat. Photonics **16**(7), 512–518 (2022).
25. Q. Bournet, F. Guichard, M. Natile, Y. Zaouter, M. Joffre, A. Bonvalet, I. Pupeza, C. Hofer, F. Druon, M. Hanna, and P. Georges, "Enhanced intrapulse difference frequency generation in the mid-infrared by a spectrally dependent polarization state," Opt. Lett. **47**(2), 261 (2022).
26. G. Barbiero, H. Wang, M. Grassl, S. Groebmeyer, D. Kimbaras, M. Neuhaus, V. Pervak, T. Nubbemeyer, H. Fattahi, and M. F. Kling, "Efficient nonlinear compression of a thin-disk oscillator to 8.5 fs at 55 W average power," Opt. Lett. **46**(21), 5304–5307 (2021).
27. K. Hashimoto, V. R. Badarla, T. Imamura, T. Ideguchi, and T. Ideguchi, "Broadband complementary vibrational spectroscopy with cascaded intra-pulse difference frequency generation," Opt. Lett. **46**(21), 5517–5520 (2021).
28. X. Feng, F. Liu, C. Ning, J. Shi, P. Liu, J. Heng, and Z. Zhang, "Broadband Mid-IR Light Sources From Difference Frequency Generators Based on a 2-mm-Long Aperiodically-Poled Lithium-Niobate Crystal," IEEE Photonics J. **13**(4), 1–5 (2021).
29. K. Tian, L. He, X. Yang, and H. Liang, "Mid-Infrared Few-Cycle Pulse Generation and Amplification," Photonics **8**(8), 290 (2021).
30. T. P. Butler, N. Lilienfein, J. Xu, N. Nagl, C. Hofer, D. Gerz, K. F. Mak, C. Gaida, T. Heuermann, M. Gebhardt, J. Limpert, F. Krausz, and I. Pupeza, "Multi-octave spanning, Watt-level ultrafast mid-infrared source," JPhys Photonics **1**(4), 044006 (2019).
31. J. Zhang, K. Fritsch, Q. Wang, F. Krausz, K. F. Mak, and O. Pronin, "Intra-pulse difference-frequency generation of mid-infrared (2.7-20 μm) by random quasi-phase-matching," Opt. Lett. **44**(12), 2986–2989 (2019).
32. R. Huber, A. Brodschelm, F. Tauser, and A. Leitenstorfer, "Generation and field-resolved detection of femtosecond electromagnetic pulses tunable up to 41 THz," Appl. Phys. Lett. **76**(22), 3191–3193 (2000).
33. A. Bonvalet, M. Joffre, J. L. Martin, and A. Migus, "Generation of ultrabroadband femtosecond pulses in the mid-infrared by optical rectification of 15 fs light pulses at 100 MHz repetition rate," Appl. Phys. Lett. **67**(20), 2907–2909 (1995).
34. R. A. Kaindl, D. C. Smith, M. Joschko, M. P. Hasselbeck, M. Woerner, and T. Elsaesser, "Femtosecond infrared pulses tunable from 9 to 18 μm at an 88-MHz repetition rate," Opt. Lett. **23**(11), 861–863 (1998).
35. R. A. Kaindl, F. Eickemeyer, M. Woerner, and T. Elsaesser, "Broadband phase-matched difference frequency mixing of femtosecond pulses in GaSe: Experiment and theory," Appl. Phys. Lett. **75**(8), 1060–1062 (1999).
36. M. Poetzlberger, J. Zhang, S. Gröbmeyer, D. Bauer, D. Sutter, J. Brons, and O. Pronin, "Kerr-lens mode-locked thin-disk oscillator with 50% output coupling rate," Opt. Lett. **44**(17), 4227–4230 (2019).
37. J. Schulte, T. Sartorius, J. Weitenberg, A. Vernaleken, and P. Russbueldt, "Nonlinear pulse compression in a multi-pass cell," Opt. Lett. **41**(19), 4511–4514 (2016).
38. J. Weitenberg, T. Saule, J. Schulte, and P. Rußbüldt, "Nonlinear Pulse Compression to Sub-40 fs at 4.5 μJ Pulse Energy by Multi-Pass-Cell Spectral Broadening," IEEE J. Quantum Electron. **53**(6), 1–4 (2017).
39. P. Balla, A. B. Wahid, and I. Sytcevich, *et al.*, "Postcompression of picosecond pulses into the few-cycle regime," Opt. Lett. **45**(9), 2572–2575 (2020).
40. M. Müller, J. Buldt, H. Stark, C. Grebing, and J. Limpert, "Multipass cell for high-power few-cycle compression," Opt. Lett. **46**(11), 2678 (2021).
41. C.-L. Tsai, F. Meyer, A. Omar, Y. Wang, A.-Y. Liang, C.-H. Lu, M. Hoffmann, S.-D. Yang, and C. J. Saraceno, "Efficient nonlinear compression of a mode-locked thin-disk oscillator to 27 fs at 98 W average power," Opt. Lett. **44**(17), 4115–4118 (2019).
42. S. Gröbmeyer, K. Fritsch, B. Schneider, M. Poetzlberger, V. Pervak, J. Brons, and O. Pronin, "Self-compression at 1 μm wavelength in all-bulk multi-pass geometry," Appl. Phys. B **126**(10), 159 (2020).
43. S. Gröbmeyer, "High-power few-cycle pulse generation towards the gigawatt frontier," Text. PhDThesis, Ludwig-Maximilians-Universität München (2022).
44. A. Baltuška, T. Fuji, and T. Kobayashi, "Controlling the Carrier-Envelope Phase of Ultrashort Light Pulses with Optical Parametric Amplifiers," Phys. Rev. Lett. **88**(13), 133901 (2002).
45. H. Fattahi, A. Schwarz, S. Keiber, and N. Karpowicz, "Efficient, octave-spanning difference-frequency generation using few-cycle pulses in simple collinear geometry," Opt. Lett. **38**(20), 4216 (2013).
46. S. A. Hussain, W. Schweinberger, T. Buberl, C. Hofer, and I. Pupeza, "Train of Ultrashort Mid-Infrared Pulses with Sub-mrad Carrier-Envelope Phase Stability," in *2019 Conference on Lasers and Electro-Optics Europe & European Quantum Electronics Conference (CLEO/Europe-EQEC)* (IEEE, 2019), p. 1.
47. R. W. Boyd, ed., *Nonlinear Optics* (3rd Edition) (Academic Press, 2008).

Optics EXPRESS

48. T. Zentgraf, R. Huber, N. C. Nielsen, D. S. Chemla, and R. A. Kaindl, "Ultrabroadband 50-130 THz pulses generated via phase-matched difference frequency mixing in $LiIO_3$," Opt. Express **15**(9), 5775–5781 (2007).
49. T. Amochkina, D. Hahner, M. Trubetskov, H. Kassab, I. Pupeza, F. Krausz, and V. Pervak, "Ultra-Broadband Near-Infrared/Mid-Infrared Beamsplitter for Bio-Medical Laser Applications," in *Optical Interference Coatings Conference (OIC) 2022 (2022)*, Paper TA.11 (Optica Publishing Group, 2022), p. TA.11.
50. L. Quaroni, "Infrared microscopy in the study of cellular biochemistry," Infrared Phys. Technol. **105**, 102779 (2020).
51. J. Zhang, K. Fai Mak, N. Nagl, M. Seidel, D. Bauer, D. Sutter, V. Pervak, F. Krausz, and O. Pronin, "Multi-mW, few-cycle mid-infrared continuum spanning from 500 to 2250 cm^{-1}," Light: Sci. Appl. **7**(2), 17180 (2018).
52. N. Karpowicz, "NickKarpowicz/LightwaveExplorer," (2023).
53. V. Petrov, A. Yelisseyev, L. Isaenko, S. Lobanov, A. Titov, and J.-J. Zondy, "Second harmonic generation and optical parametric amplification in the mid-IR with orthorhombic biaxial crystals $LiGaS_2$ and $LiGaSe_2$," Appl. Phys. B: Lasers Opt. **78**(5), 543–546 (2004).
54. D. N. Nikogosyan, *Nonlinear Optical Crystals: A Complete Survey*, 2005th edition (Springer, 2005).
55. G. Ghosh, "Dispersion-equation coefficients for the refractive index and birefringence of calcite and quartz crystals," Opt. Commun. **163**(1-3), 95–102 (1999).
56. D. A. Roberts, "Simplified characterization of uniaxial and biaxial nonlinear optical crystals: a plea for standardization of nomenclature and conventions," IEEE J. Quantum Electron. **28**(10), 2057–2074 (1992).
57. J. Valdmanis and G. Mourou, "Subpicosecond electrooptic sampling: Principles and applications," IEEE J. Quantum Electron. **22**(1), 69–78 (1986).
58. Q. Wu and X. -C. Zhang, "Free-space electro-optic sampling of terahertz beams," Appl. Phys. Lett. **67**(24), 3523–3525 (1995).
59. A. Leitenstorfer, S. Hunsche, J. Shah, M. C. Nuss, and W. H. Knox, "Detectors and sources for ultrabroadband electro-optic sampling: Experiment and theory," Appl. Phys. Lett. **74**(11), 1516–1518 (1999).
60. C. Kübler, R. Huber, S. Tübel, and A. Leitenstorfer, "Ultrabroadband detection of multi-terahertz field transients with GaSe electro-optic sensors: Approaching the near infrared," Appl. Phys. Lett. **85**(16), 3360–3362 (2004).
61. M. Knorr, P. Steinleitner, J. Raab, I. Gronwald, P. Merkl, C. Lange, and R. Huber, "Ultrabroadband etalon-free detection of infrared transients by van-der-Waals contacted sub-10-µm GaSe detectors," Opt. Express **26**(15), 19059 (2018).
62. P. Maslowski, K. F. Lee, A. C. Johansson, A. Khodabakhsh, G. Kowzan, L. Rutkowski, A. A. Mills, C. Mohr, J. Jiang, M. E. Fermann, and A. Foltynowicz, "Surpassing the path-limited resolution of Fourier-transform spectrometry with frequency combs," Phys. Rev. A **93**(2), 021802 (2016).
63. A. V. Muraviev, V. O. Smolski, Z. E. Loparo, and K. L. Vodopyanov, "Massively parallel sensing of trace molecules and their isotopologues with broadband subharmonic mid-infrared frequency combs," Nat. Photonics **12**(4), 209–214 (2018).
64. P. Sulzer, M. Högner, A.-K. Raab, L. Fürst, E. Fill, D. Gerz, C. Hofer, L. Voronina, and I. Pupeza, "Cavity-enhanced field-resolved spectroscopy," Nat. Photonics **16**(10), 692–697 (2022).
65. P. Hamm and M. Zanni, *Concepts and Methods of 2D Infrared Spectroscopy*, 1st ed. (Cambridge University, 2011).
66. C. Manzoni, O. D. Mücke, G. Cirmi, S. Fang, J. Moses, S.-W. Huang, K.-H. Hong, G. Cerullo, and F. X. Kärtner, "Coherent pulse synthesis: towards sub-cycle optical waveforms," Laser Photonics Rev. **9**(2), 129–171 (2015).
67. P. Merkl, M. Knorr, C. Meineke, L. Kastner, D. Peller, and R. Huber, "Multibranch pulse synthesis and electro-optic detection of subcycle multi-terahertz electric fields," Opt. Lett. **44**(22), 5521–5524 (2019).
68. "HITRAN on the Web," https://hitran.iao.ru/home.sim-theory.sp-functions.
69. T. Kawamori, P. G. Schunemann, and K. L. Vodopyanov, "High-order mid-IR multiphoton absorption and nonlinear refraction in GaP, ZnSe, GaSe, and ZGP crystals," in *Conference on Lasers and Electro-Optics (2021)*, Paper STu4C.1 (Optica Publishing Group, 2021), p. STu4C.1.
70. B.-H. Chen, T. Nagy, and P. Baum, "Efficient middle-infrared generation in $LiGaS_2$ by simultaneous spectral broadening and difference-frequency generation," Opt. Lett. **43**(8), 1742–1745 (2018).
71. Q. Bournet, M. Jonusas, A. Zheng, F. Guichard, M. Natile, Y. Zaouter, M. Joffre, A. Bonvalet, F. Druon, M. Hanna, and P. Georges, "Inline amplification of mid-infrared intrapulse difference frequency generation," Opt. Lett. **47**(19), 4885–4888 (2022).